Highlights

Pleistocene shifts in Great Basin hydroclimate seasonality govern the formation of lithium-rich paleolake deposits

Tripti Bhattacharya, Peter R. Brennan, Daniel E. Ibarra, Catherine A. Gagnon, Kristina L. Butler, Alexa Terrazas, Shaw Miller, Lee Ann Munk, David F. Boutt, Ran Feng, Stephanie N. Bullinger, Lucy Weisbeck

- Leaf wax hydrogen isotopes from the Plio-Pleistocene southern Great Basin reveal a reduction in winter rainfall between 2.6 and 2.2 Ma
- Early Pleistocene fluctuations in winter rainfall were likely driven by shifts in the meridional sea surface temperature gradient in the Pacific
- Shifts in past hydroclimate likely played an integral role in the formation of lithium-rich lacustrine clay deposits in western North America

Pleistocene shifts in Great Basin hydroclimate seasonality govern the formation of lithium-rich paleolake deposits

Tripti Bhattacharya[a], Peter R. Brennan[a], Daniel E. Ibarra[b], Catherine A. Gagnon[b], Kristina L. Butler[b,d], Alexa Terrazas[c], Shaw Miller[b], Lee Ann Munk[e], David F. Boutt[f], Ran Feng[g], Stephanie N. Bullinger[a], Lucy Weisbeck[a]

[a]*Department of Earth and Environmental Sciences, Syracuse University,*
[b]*Department of Earth, Environmental and Planetary Science, Brown University,*
[c]*Department of Atmospheric and Oceanic Sciences, University of California Los Angeles,*
[d]*Department of Sustainable Earth Systems Sciences, The University of Texas at Dallas,*
[e]*Department of Geological Sciences, University of Alaska-Anchorage,*
[f]*Department of Geosciences, University of Massachusetts-Amherst,*
[g]*Department of Earth, Geographic, and Climate Sciences, University of Connecticut,*

Abstract

Southwestern North America is currently experiencing a multidecadal megadrought, with severe consequences for water resources. However, significant uncertainty remains about 21st century precipitation changes in this semi-arid region. Paleoclimatic records are essential for both contextualizing current change, and for helping constrain the sensitivity of regional hydroclimate to large-scale global climate. In this paper, we present a new 2.8 Ma to present compound-specific isotopic record from Clayton Valley, the site of a long-lived paleolake in the southern Great Basin. Hydrogen and carbon isotopes from terrestrial plant leaf waxes provide evidence of past shifts in rainfall seasonality as well as ecosystem structure, and help contextualize the formation of this lithium-rich lacustrine basin. Our results suggest that regional hydroclimates underwent a substantial reorganization at the Plio-Pleistocene boundary, especially between 2.6 and 2.0 Ma. In this interval, a reduced latitudinal temperature gradient in the North Pacific likely resulted in a northward shift in storm tracks, and a reduction in winter rainfall over the southern Great Basin. This occurred against a background of increased summer rainfall and a greater accumulation of lithium in the lake basin. Our interpretation is corroborated by a compilation of Plio-Pleistocene north Pacific sea surface temperature records, as well as an isotope-enabled model simulation. Overall, these results suggest that past shifts in rainfall seasonality helped set the stage for the development and dessication of lithium-rich lacustrine deposits.

Keywords: Plio-Pleistocene, southwest North America

PACS: 0000, 1111

2000 MSC: 0000, 1111

---

1. Introduction

Southwestern North America is currently in the midst of an ongoing megadrought that has resulted in reductions in water resources, snowpack, and an increase in related hazards like wildfire. Although megadroughts have occurred in this region historically, anthropogenic emissions have likely exacerbated the risk of 21st century megadrought (Williams et al., 2020). While increases in temperature play a key role in increasing 21st century drought (King et al., 2024), rainfall remains much more uncertain. Southwestern North America features a bimodal rainfall distribution: the region receives rainfall from the North American Monsoon (NAM) in summer, while midlatitude storms provide rainfall in the winter.

The future behavior and relative contribution of both these precipitation regimes remains unclear (Choi et al., 2016; Almazroui et al., 2021). State-of-the-art Earth System Models (ESMs) disagree about the future response of the NAM to anthropogenic warming, which may result from models' persistent sea surface temperature (SSTs) biases in the North Pacific, as well as the inability of coarse-resolution models to resolve the details of moist convection associated with the monsoon (Cook and Seager, 2013; Pascale et al., 2017; Almazroui et al., 2021; Wallace and Minder, 2024). Similarly, model disagreement about the future behavior of winter precipitation stems in part from model disagreement about future large-scale changes in circulation over the North Pacific (Choi et al., 2016).

In the face of this uncertainty, paleoclimatic data can help constrain the sensitivity of southwest hydroclimates to large-scale climate forcings. Evidence from past greenhouse climates, including the Pliocene, the last interval in Earth history when CO_2 was above pre-industrial levels, has helped constrain the response of southwestern hydroclimates to a warmer background climate state. Proxy evidence from the Pliocene suggests that the NAM was stronger between 3.5 and roughly 2.0 Ma, and could have contributed to increased lake levels and more mesic vegetation in the southwest (Bhattacharya et al., 2022). Modeling experiments with Pliocene boundary conditions have also helped clarify how other phenomena like atmospheric rivers respond to changes in topography and geography, as well as altered SST patterns (Menemenlis et al., 2021; Brennan et al., 2022). However, while there is some suggestion that long-term changes in winter storms could have driven higher lake levels in the Pliocene, it remains unclear how winter storm tracks over the eastern Pacific and western North America responded to global cooling over the Plio-Pleistocene transition (Ibarra et al., 2018; Peaple et al., 2024).

Here, we present new evidence of late Pliocene and early Quaternary hydroclimate shifts recorded in lake sediments from Clayton Valley, a paleolake basin in Nevada that is currently the site of a lithium brine operation. Understanding the evolution of this lake basin therefore has the potential to shed light on the environmental conditions that help concentrate lithium, an element critical to the energy transition, in sedimentary environments such as Clayton Valley and other locations (Vine, 1975; Davis et al., 1986; Gagnon et al., 2023; Benson et al., 2023). We present new stable hydrogen and carbon isotopes in long-chain terrestrially derived leaf waxes in a sediment core that spans the interval from the late Pliocene, 2.8 Ma, and continues until the present-day.

Previous geochemical data has helped clarify the history of aridity in this basin, as well as how climate contributed to the formation of lithium-rich clays in the basin (Coffey et al., 2021; Gagnon et al., 2023). However, leaf wax isotopes provide a novel perspective, since hydrogen isotopes in these long-chain alkyl compounds have been shown to have a strong correlation with the hydrogen isotopic composition of precipitation, while carbon isotopes reflect large-scale ecosystem structure (Sachse et al., 2012; Inglis et al., 2022). Late Pleistocene leaf wax records from the southwest show similar patterns of change to high-resolution speleothem records, and prior work has shown that hydrogen isotopes in leaf waxes show a strong correlation with the relative amount of summer vs.

winter rainfall in the southwest (Peaple et al., 2022; Bhattacharya et al., 2018). We therefore use these data to assess how changes in winter storms, or summertime moisture, contributed to the evolution of hydroclimate at Clayton Valley over the Plio-Pleistocene transition. This allows us to test if precipitation seasonality changes may have influenced lithium delivery, via weathering and solute generation and concentrating processes to the paleolake. We complement these data with analysis of previously published regional sea surface temperature records as well as climate model simulations in order to evaluate the large-scale controls on changes in hydroclimate in the desert southwest.

2. Background and Methods

2.1. Geological and Climatological Setting

Clayton Valley (CV) is a topographically closed, half-graben basin in the Basin and Range Province (Vine, 1975; Davis et al., 1986; Coffey et al., 2021; Gagnon et al., 2023) (Figure 1). Currently, the basin is a source of lithium (Li) from brines rich in the element (Munk et al., 2016). The Clayton Valley playa sits at an elevation of 1400 masl, and is 30 km to the northwest of Death Valley. Although much of the uplift in this region occurred prior to the early Pliocene, evidence suggests that the elevation ranges of nearby mountain ranges, including the central Sierra Nevada, were established between 1 and 3 Ma, creating a rain-shadow to the west of CV (Thompson, 1991; Mix et al., 2019). Currently, vegetation in the valley consists of sparse sagebrush (*Artemisia* spp.) and creosote (*Larrea* spp.), with nearby mountain regions containing a mix of oak (*Quercus* spp.), juniper (*Juniperus* spp.), and other conifers. While potential evapotranspiration exceeds precipitation in the southern Great Basin, the region does receive roughly 13 cm of rainfall a year (Munk and Chamberlain, 2011).

Rainfall in CV derives from two distinct seasonal sources. The valley receives the majority of its rainfall in winter, when the jet over the eastern Pacific steers storms towards the west coast of North America (Gagnon et al., 2023). However, approximately 20-30% of annual rainfall at CV also derives from the summer monsoon, when surges of monsoonal moisture from the south extend into regions of the southern Great Basin (Bhattacharya et al., 2023). These sources of moisture have distinct isotopic signals: a nearby isotope monitoring station (NV-00) reveals that summertime (June-August) rainfall has a hydrogen isotopic value of roughly $-50‰$, while winter (October - December) rainfall is closer to $-100‰$. Data from NV-00 provides monthly amount-weighted precipitation data, and is obtained from Welker (2012). The dataset was collected between 1989 and 1995. The relative enrichment of summer compared to winter rainfall is also well documented in other sources (Eastoe and Dettman, 2016; Aggarwal et al., 2016; Friedman et al., 2002). The complex topography of the Sierra Nevada blocks atmospheric circulation, resulting in site by site variations in the relative proportions of summer or winter moisture that reach leeward sites like CV (Lechler and Galewsky, 2013).

2.2. Sedimentology and Age Model

Drill core EXP2 was drilled between June and November 2017 by commercial Li mining operations (Albemarle Corporation) in the CV basin. The core is 990.6 m in length, and detailed information on the sedimentology of the core as well as its environmental interpretation, is available in Gagnon et al. (2023) and Coffey et al. (2021) (Figure 2). From 990.6-896.7 m, the EXP2 core consists of alluvium of angular gravel with siltstone clasts and a basal lithic tuff. Between 896.7 and 535.0 and m, perennial lake sediments are green clay and thin volcanic ash layers. At 535.0 to 405.4 m, the core contains shallow to desiccated lake sediments characterized by a thick layers of halite interbedded with thin layers of clay. Between 405 and 228.6 m, the core consists a second perennial lake interval of brown and green clays with layers of silty clays. The upper 228.6 m of the core consists of sands and gravels, transitioning to clays with thin infrequent sand layers interpreted as a shallow lake transitioning into the present day playa setting (Figure 2).

The age model for the site is based on 5 previously published argon-argon dates from sanidine/plagioclase as well as a zircon U-Pb age (Coffey et al., 2021; Gagnon et al., 2023) (Figure 2). The age model was constructed using Bayesian age modeling techniques following Blaauw et al. (2018) in Gagnon et al. (2023), and the line of best fit for the available ages is linear, with a constant slope (e.g. sediment accumulation rate). Because of the age uncertainty in this record (e.g. 1-σ age uncertainty is roughly 50 ka thoughout the record), we are unable to resolve orbital scale variability. Despite this, the CV record represents one of the only well-dated lacustrine cores spanning the Plio-Pleistocene transition from southwest North America.

2.3. *Leaf Wax Analyses*

Leaf waxes were extracted using standard protocols (Sachse et al., 2004; Chikaraishi and Naraoka, 2006). This involved an initial step of sediment lyophilization, homogenization, and extraction of the total lipids using an accelerated solvent extractor (ASE 350, Dionex). Our analyses focus on leaf wax fatty acids, which were eluted using a mix of dichloromethane and isopropanol, and then using a 5% acetic acid in dichloromethane solution over aminopropyl gel. To eliminate exchangeable hydrogen in the molecule, leaf wax *n*-acids were methylated using a methanol standard of known isotopic composition to create fatty acid methyl esters (FAMEs). Concentrations of fatty acids were determined using a Trace 1310 GC-FID. These data were also used to calculate the Carbon Preference Index (CPI) and the Average Chain Length (ACL). CPI measures the extent to which fatty acids maintain an even-over-odd preference, while ACL represents a concentration-weighted average chain length of the wax compounds found in a sample.

We quantified the hydrogen and carbon isotopic composition of the three most abundant long chain FAMEs (C_{26}; C_{28}; and C_{30}) via gas chromatograph - isotope ratio mass spectrometry (GC-IR-MS). This consists of a Thermo Delta V Plus mass spectrometer coupled to a Trace 1310 GC-FID, using either a pyrolysis (H_2) or combustion reactor (CO_2). H_2 and CO_2 gases calibrated to an external *n*-alkane standard (A7 mix provided by Arndt Schimmelmann at Indiana University) provided references for each analysis. An internal isotopic standard consisting of a synthetic mix of FAMEs was analyzed every 5-7 samples to monitor (and subsequently correct for) instrument drift. Samples were run in triplicate for δD to obtain a precision better than $2\,‰$ (1σ), and in duplicate or triplicate for δ^{13}C to obtain a precision better than $0.2\,‰$ (1σ). Over the course of the run, precision for internal standard measurements was similarly $2\,‰$ (1σ) for hydrogen and $0.2\,‰$ (1σ) for carbon. Leaf wax values are not corrected for ice volume changes (Schrag et al., 1996; Lisiecki and Raymo, 2005; Westerhold et al., 2020) to remain consistent with previous Plio-Pleistocene leaf wax studies in the region (Bhattacharya et al., 2022; Peaple et al., 2024).

2.4. Inferring δD of Precipitation

δD_{wax} values are generally offset from the isotopic value of environmental waters or mean annual precipitation or δD_p. ε_{p-w}, otherwise known as apparent fractionation, is known to vary systematically across plant clades. Graminoids (e.g. grasses) have a larger ε_{p-w} (e.g. are more depleted relative to δD_p), than eudicots, which likely reflects differences in leaf wax biosynthesis and leaf development (Gao et al., 2014). Following our previous work (e.g. (Bhattacharya et al., 2022, 2018), we use a Bayesian mixing model and $\delta^{13}C_{wax}$ data to infer the proportion of waxes in a sample that derive from C_4 grasses, since C_4 plants have a more enriched carbon isotopic signature than C_3 plants (Collister et al., 1994). End-member constraints on C_4 grasses and C_3 eudicots come from modern plant waxes included in previously published compilations (Sachse et al., 2012; Liu and An, 2020). Because these constraints are primarily available for the longest chain length (e.g. the C_{29} alkane and the C_{30} *n*-acid), we infer δD_p from the hydrogen isotopic signature of the C_{30} *n*-acid.

Our analyses incorporate the full range of possible measurements of $\delta^{13}C_{wax}$. Briefly, we use Monte Carlo resampling methods to sample our end members for C_3 eudicots and C_4 grasses from a normal distribution that incorporates full range of uncertainty in C_3 $\delta^{13}C_{wax}$ and C_4 $\delta^{13}C_{wax}$ values, respectively, available in prior compilations. We then use these to infer a range of values for fraction of C_4 plants contributing to a sample (f_{C4}) for each measurement down-core. This inference is done in a Bayesian framework following the methods in Tierney et al. (2017) and Bhattacharya et al. (2018). Because of the large range of compiled $\delta^{13}C_{wax}$ values for C_4 grasses and C_3 eudicots, the uncertainty in our inference of f_{C4} is larger than any trends in the overall data (Figure S3). We then use the proportion of inferred C_4 vegetation to determine the appropriate ε_{p-w} to apply to a given sample:

$$\epsilon = f_{C4} \cdot \epsilon_{C4} + (1 - f_{C4}) \cdot \epsilon_{C3} \quad (1)$$

We use the full range of ε_{p-w} that were obtained from δD_{wax} measured on the Arizona-Sonora Desert Museum inBhattacharya et al. (2022), as well as constraints from Sachse et al. (2012)). The approach involves weighting the value of ε_{p-w} for C_3 and C_4 plants by the inferred fraction of C_3 and C_4 plants in the sample (Equation 1). Because all calculations are performed in a Bayesian framework, uncertainties are propagated through all steps of the calculation (e.g. we iteratively sample through the full distribution of f_{C4} values and then the full distribution of ε_{p-w} values). While our initial 1σ precision for δD_w measurements is 2‰, 1σ uncertainty for our final estimate of δD_p is 5-6‰. This Bayesian approach has been previously used to study paleohydrological signals in leaf waxes (Tierney et al., 2017; Windler et al., 2023), including within the NAM domain (Bhattacharya et al., 2018, 2022). The correction procedure for vegetation effects, in the case of this record, does not alter the overall signal in our δD_{wax} data: our inferred δD_p signal is highly correlated with the δD_{wax} (r = 0.94). After inferring Plio-Pleistocene changes in δD_p from the C_{30}, we compare these results to previously published leaf wax hydrogen isotope records from the desert southwest.

2.5. Carbonate Isotopes and Bulk Lithium Concentrations

135 new carbonate oxygen and carbon isotope measurements, as well as 36 new lithium concentration measurements, are reported in this work. These data extend the record presented in Gagnon et al. (2023) and Coffey et al. (2021). For carbonate oxygen and carbon analyses, bulk core samples were homogenized using a ceramic mortar and pestle and reacted with 70°C phosphoric acid under vacuum using a Kiel IV carbonate device with the evolved carbon dioxide measured on a Thermo Scientific 253 Plus 10 kV Isotope Ratio Mass Spectrometer (Gagnon et al., 2023). External precision ($1\ \sigma$) for both $\delta 18O_w$ and $\delta 13C_w$ was <0.1‰ based on repeat measurements of two internal marble standards were

calibrated against international recognized standards (Gagnon et al., 2023). For lithium measurements, as in previous work (Gagnon et al., 2023; Coffey et al., 2021), whole-rock samples were analyzed by SGS Environmental Services by inductively coupled plasma-optical emission spectrometry (ICP-OES). In brief, 0.1g of crushed and dried sample was fused using Na_2O_2 and digested in HCl. The digested solution was analyzed on an Agilent ICP-OES. The core samples measured for new lithium concentrations are paired to newly reported (n=11) or previously reported (n=25) measured carbonate oxygen and carbon isotope measurements. New carbonate isotope and lithium data confirm the overall trends presented in prior work, largely confirming the temporal pacing of wet and dry intervals presented in Gagnon et al. (2023).

3. Results

3.1. Leaf Wax Results

CV EXP2 leaf waxes show remarkably stable CPI and ACL values, and indicate limited alteration of terrestrially-derived waxes. CPI values are consistently above 3, indicating a predominantly even-over-odd preference for leaf wax fatty acids (Figure S1). ACL values are also very stable over the record, and consistently range between 26 and 28, indicating that long-chain waxes dominate the sample. Based on these results, we analyze the carbon and hydrogen isotopic composition of three chain lengths of *n*-acid (C_{26}; C_{28}; and C_{30}).

The carbon isotopic composition of all three chain lengths are strongly correlated (Table S1). For all three chain lengths, carbon isotopic values vary between approximately -30 and -24‰VPDB (Figure 3). Between 3 and 2 Ma, the carbon isotopic signature of C_{26}, C_{28}, and C_{30} becomes more positive, increasing to roughly -25‰ from -29‰. After this point, values remain relatively stable, fluctuating near -24‰ until 0.5 Ma, after which they show higher amplitude fluctuations.

Similar to carbon, the δD signature of all three chain lengths are strongly correlated (Table S1), and show similar long-term trends over the Plio-Pleistocene transition. Between 2.8 and 2.5 Ma, all chain lengths exhibit a shift towards more positive δD values, peaking at roughly 2.3 Ma, before declining by 2 Ma (Figure 3). This excursion is much more pronounced in the C_{26} *n*-acid compared to C_{28} and C_{30}. A shift to more positive values is also evident in the oxygen isotope values of authigenic carbonates from EXP2 and coincides with an increase in the concentration of lithium in bulk sediments (Gagnon et al., 2023). Li concentrations peak at 2.5 Ma, and then decline by 2.0 Ma, similar to the timing of the shift in carbonate and leaf wax isotopic values. After roughly 1.5 Ma, values of each leaf wax fluctuate between -160 and -180‰. We note that C_{26} is slightly more enriched in deuterium than the other two chain lengths of *n*-acid (Figure 3).

The CV EXP2 δD_p record, inferred from the C_{30} *n*-acid, fluctuates between -60 and -100‰VSMOW, apart from one basal outlying value (Figure 5). The most modern values are between -80 and $-100\,‰$VSMOW, similar to modern winter values of δD_p from the NV-00 station (Figure 1, 5). This observation increases our confidence that our approach to reconstructing δD_p, especially our choice of ε_{p-w}, yields reasonable results. We compare the EXP2 δD_p reconstruction to two other continuous Plio-Pleistocene leaf wax records from the southwest that both extend back to 3.5 Ma (Figure 4). The leaf wax-inferred δD_p record from CV exhibits some similar features to the two available leaf wax records from the region from ODP 1012 on the southern California margin and DSDP 475 off Baja California. Notably, all three records show a decline in δD_p between 2.9 and 2.75 Ma and all three records show increasing δD_p between 2.6 and 2.3 Ma, followed by a decline between roughly 2.3 and 2.0 Ma (Figure 5). We also note that a recently-published record from Searles Lake does not cover this entire interval, but does show a shift towards more positive δD_p values between 2.8 and 2.6 Ma, potentially in agreement with the pattern seen at CV (Peaple et al., 2024). Both CV and Searles Lake also show similar reconstructed late Pliocene δD_p values of between -80 and$-70\,‰$, further increasing confidence in our approach (Peaple et al., 2024).

4. Discussion

4.1. Plio-Pleistocene ecosystem change in the southern Great Basin

At an ecosystem scale, leaf wax carbon isotopes reflect changes in the relative proportion of plants using the C_3 vs. C_4 photosynthetic pathways on the landscape, or could reflect shifts in water use efficiency. With this context, the trend towards more positive $\delta^{13}C$ values between 3 and 2 Ma in all three chain lengths of leaf wax *n*-acids likely reflects a small increase in the representation of plants using the C_4 photosynthetic pathway in the southern Great Basin. This could reflect an increase in the proportion of C_4 grasses on the landscape. However, recent work combining pollen and leaf wax carbon isotopes found that in some regions of the arid southwest, a more C_4-like signature can actually reflect a greater proportion of phreatophytic shrubs using the C_4 photosynthetic pathway, like *Atriplex* (Peaple et al., 2024, 2022). The increase in $\delta^{13}C$ values values in the CV record may therefore reflect long-term shifts to either more C_4 grasses, or an increase in shrubs indicative of regional shifts in water tables.

Other biomarker or pollen evidence would be needed to provide clear evidence of a vegetation shift, and we cannot rule out shifts in water use efficiency. However, we tentatively suggest that the long-term shift in carbon isotopes reflects a greater proportion of C_4 grasses on the landscape as a result of greater aridity, and a decrease in winter rainfall. Ecological literature from the Great Basin suggests that reduced winter rainfall can favor the expansion of shallow-rooted plants that include, but are not limited to, perennial C_4 grasses that facultatively use a greater portion of summer moisture (Donovan and Ehleringer, 1994). In addition, C_4 photosynthesis tends to have a competitive advantage in warm, semi-arid habitats (Sage et al., 1999). This conceptual model is supported by longer-term Cenozoic records of habitat expansion, which found that C_4 grasslands expanded with aridification in western-central North America (Kukla et al., 2022). Because we have independent evidence of a progressive reduction in winter rainfall until roughly from 2.6 to roughly 2.0 Ma (see section 4.2), we suggest that this likely resulted in an expansion of C_4 grass habitats at the expense of woodland or shrub environments in the southern Great Basin.

4.2. Shifts in Rainfall Seasonality Between 2.6 and 2.2 Ma

The CV leaf wax-inferred δD_p record shows an excursion to values near -60 ‰ between 2.6 an 2.0 Ma, after which time values of δD_p return to approximately -95 ‰. A similar excursion to more positive δD_p values is observed at ODP 1012, though overall values of δD_p at this site are more enriched than at CV (Figure 5). This likely reflects this site's proximity to the coast, while CV is located in the lee side of the Sierra Nevada and the White Mountains, meaning that westerly air masses that first begin to rain on the coast near site 1012 undergo significant vapor distillation before reaching CV (Lechler and Galewsky, 2013; Mix et al., 2019). There is significant uncertainty associated with the CV age model: between 2.6 and 2.0 Ma, the 1-σ age uncertainty associated with each leaf wax measurement is roughly 50 ka. Therefore, the timing of the positive excursion in δD_p at CV remains uncertain, and the change of roughly 30 ‰ in this interval is relatively modest given the variability present in the record. However, the fact that all three regional records switch to increasing δD_p values at roughly 2.6 Ma bolsters our argument that it is a robust feature of the regional paleoclimatic record.

We interpret a shift to more enriched δD_p values at CV as indicating a reduced contribution of winter rainfall relative to summer rainfall. In the desert southwest, summer rainfall is more enriched in deuterium than winter rainfall (Figure 1). This is likely because winter precipitation tends to have a greater proportion of large-scale stratiform rainfall, compared to the summer, which tends to feature more isotopically enriched deep convective rainfall (Aggarwal et al., 2016; Schumacher and Funk, 2023). Other processes (e.g. large-scale shifts in moisture source, sub-cloud re-evaporation, vapor recycling, and proximity to moisture source) may also enhance the seasonal difference in precipitation isotopes (Eastoe and Dettman, 2016; Bhattacharya et al., 2022). From this perspective, the positive excursion in δD_p values between 2.6 and 2.0 Ma could reflect a reduction in winter rainfall to the CV region, resulting in a proportionally greater proportion of summer rainfall. A positive excursion between 2.6 and 2.0 Ma also exists in δ^{18}O of authigenic lacustrine carbonates from CV (Figure 3). This shift in lacustrine carbonate isotopes could corroborate the reduction in winter moisture delivery and/or could reflect greater aridity, which would result in greater evaporative demand from the lake basin.

Non-climatic factors could certainly also have influenced the Clayton Valley δD_p record. Quaternary orographic changes (e.g. uplift of the White Mountains and the Sierra Nevada) could result in a change in moisture trajectories, or the degree of orographic rainout of winter storms, upstream from Clayton Valley. This would likely result in a long-term depletion trend in the CV record, but would not necessarily influence coastal records like ODP 1012. However, long-term changes in orographic rainout is unlikely to result in a distinct, temporally constrained *increase* in δD_p between 2.6 and 2.0 Ma, suggesting that this excursion is likely driven by climate.

Prior work has shown that summer rainfall in the southwest was higher in the Pliocene, declining between 3.0 Ma and until roughly 2.25-2.5 Ma (Bhattacharya et al., 2022). The interval between 2.6 and 2.0 Ma therefore likely had slightly higher summertime rainfall than the late Pleistocene. We posit, however, that the excursion between 2.6 and 2.0 Ma is not just the result of summer rainfall changes, but also contains a signal related to a decrease in *independent* wintertime precipitation, which would further amplify the proportional contribution of summer rainfall to the annual rainfall budget. We next assess whether large-scale climate conditions between 2.6 and 2.2 Ma are consistent with a decrease in winter rainfall in this interval.

4.3. Large-Scale Changes between 2.6 and 2.2 Ma

Previous work, using a combination of models, observational data, and proxies, suggests that long-term summertime precipitation changes in the southwest is driven by the gradient of SST between the California margin and the eastern equatorial Pacific cold tongue (Bhattacharya et al., 2022, 2023). In contrast, other climatic processes, especially at high latitudes, are critical drivers of the delivery of winter rainfall by the midlatitude storm tracks. The position of the Aleutian Low (AL) and the North Pacific Subtropical High (NPSH), semi-permanent centers of low and high pressure respectively, modulate winter storm activity over western North America (Giamalaki et al., 2021; Menemenlis et al., 2021). SST variability in the equatorial Pacific, as well as extratropical modes of SST variability like the Pacific Decadal Oscillation, influence the position, intensity, and frequency of landfalling storms that impact western North America (Giamalaki et al., 2021; Gan et al., 2017; Beaudin et al., 2023). From this perspective,large-scale changes in SST patterns between 2.6 and 2.2 Ma could help bolster our argument about a shift in rainfall seasonality between 2.6 and 2.0 Ma.

We note some evidence of warmer temperatures in the northeast Pacific between 2.6 and 2.0 Ma. An SST record from site U1417 in the Gulf of Alaska shows an excursion to temperatures above 10°C between roughly 2.6 and and 2.0 Ma (Sánchez-Montes et al., 2020) (Figure 6). In addition, an alkenone-based SST record from Site 882, located in the western Bering Sea, shows a shift to slightly warmer temperatures between 2.7 and 1.7 Ma (Yamamoto and Kobayashi, 2016) (Figure 6). However, this high latitude warming does not likely reflect a canonical warm PDO-like pattern, which would involve warm SST anomalies extending down the west coast of North America. Farther south, sites on the northern California Margin do not show an excursion to warmer temperatures in this time period (LaRiviere et al., 2012; Brennan et al., 2022). Instead, sites like 1012, 1014, and 1010 show intensifying orbital-scale variability without any evidence of a mean shift to warmer values between 2.0 and 2.6 Ma (Dekens et al., 2007; Brierley et al., 2009). This suggests that warm SST anomalies in the Bering Sea and Gulf of Alaska are not the result of a persistent warm PDO-like state. We also note that there is no significant excursion in temperatures in the eastern equatorial Pacific cold tongue between 2.0 and 2.6 Ma (Figure S2; Tierney et al. (2019)). Therefore, the limited existing SST records suggest the presence of some high latitude cooling in the north Pacific, relaxing the meridional temperature gradient over the northeastern Pacific, with impacts on rainfall anomalies over western North America.

We compile a suite of SST records from across the north and equatorial Pacific in order to assess whether latitudinal SST gradients weaken between 2.6 and 2.2 Ma (Liu et al., 2019; Seki et al., 2012; Rousselle et al., 2013; Shaari et al., 2013; Etourneau et al., 2010; Herbert et al., 2016; Lawrence et al., 2006; LaRiviere et al., 2012; Dekens et al., 2007; Brierley et al., 2009; Sánchez-Montes et al., 2020; Yamamoto and Kobayashi, 2016; Brennan et al., 2022). All these records are based on the alkenone paleothermometer, which uses the ratio of di- to tri- unsaturated long-chain ketone compounds produced by haptophyte algae to quantitatively reconstruct SSTs (Herbert and Schuffert, 2000; Tierney and Tingley, 2018). We recalibrated each record using the latest Bayesian calibration (Tierney and Tingley, 2018), and interpolated values to a common 0.2 Ma timestep. We then took average SST anomalies between 2.8 and 2.6 Ma, prior to the positive excursion in our leaf wax δD_p values, and between 2.3 and 2.4 Ma, within the interval where we see a shift to more positive values in leaf wax δD_p. We also evaluate the strength of this gradient between 1.5 and 1.7 Ma in order to see whether it steepens or continues to relax following the excursion in δD_p (Figure S3).

We find that the interval between 2.3 and 2.4 Ma, when compared to the prior (2.6-2.8 Ma) and subsequent (1.7 to 1.6 Ma) interval, exhibits a shallower gradient of meridional gradient of temperature between 30 and 60° N. Between 2.8 and 2.6 Ma, we see that the north Pacific exhibits a meridional temperature gradient of

-0.58°C per ° latitude, similar to the slope seen between 1.6 and 1.7 Ma (-0.52°C per ° latitude) (Figure 7). However, between 2.3 and 2.4 Ma we find evidence of a shallower meridional temperature gradient of -0.44°C per ° latitude, a change that is significant at the 95% confidence interval (2-sided t-test) (Figure 7). This shallower gradient is primarily driven by excursions to warmer temperatures at sites like U1417 and ODP 882, coupled with strong cooling at subtropical sites like 1012 and 1014.

This shift in the latitudinal gradient is constrained by relatively few sites at high northern latitudes. Prior work also suggests that several sites may primarily reflect summer or fall SSTs, rather than an annually averaged signal. However, some sediment trap work near site 882 suggests that alkenone-based SSTs at this site may represent late fall (November) temperatures (Sánchez-Montes et al., 2020; Yamamoto and Kobayashi, 2016; Harada et al., 2006). Despite the uncertainties associated with the sparse north Pacific SST record, our results suggest that the meridional temperature gradient over the Pacific is shallower during start of the Pleistocene (e.g. 2.6 to 2.0 Ma) compared to late Pliocene (3.0 to 2.7 Ma). This runs counter to the general assumption that the meridional SST gradient should steepen in response to global cooling and glacial intensification over the Plio-Pleistocene transition. While the causes of this shift remain mysterious and are outside the scope of the current work, it is possible that they are related to shifts in deep ocean circulation in the Pacific (Burls et al., 2017). We next explore the potential consequences of a weakened latitudinal gradient for regional hydroclimate in western North America.

4.4. Dynamical Mechanisms

Between 2.6 and 2.0 Ma, warm SSTs in the high-latitude Pacific likely reduced the intensity of winter storms hitting the central-west coast of North America. Modern observations suggest that cool SST anomalies in the Gulf of Alaska and Bering Sea in late summer and early fall often persist into winter and help enhance winter storm tracks to the north of 30°N. This is because cool high latitude SSTs amplify the meridional gradient of temperature, increasing baroclinicity and cyclogenesis over the northeast Pacific (Pickart et al., 2009; Gan and Wu, 2013). Idealized model simulations show that a steeper meridional SST gradient over the north Pacific increases transient eddy activity and strengthens the polar (eddy-driven) jet (Wang et al., 2019). From this perspective, the warming of the Bering Sea and Gulf of Alaska would reduce baroclinicity and storm activity, reducing the winter storms in southwestern North America. This reduction in winter rainfall would likely also influence ODP 1012, which is located near 30°N, but would likely not have a major influence on DSDP 475, which is farther south (Figure 4). This could explain the shift to more enriched δD_p values, indicative of a reduction in winter storm activity, most prominently at CV and ODP 1012. High latitude temperatures may also influence summer rainfall, but prior work suggests that subtropical temperatures are more important in governing monsoon strength (Bhattacharya et al., 2022, 2023).

To further explore the dynamical linkage between north Pacific temperatures and hydroclimate in the region around CV, we analyze two simulations of the isotope-enabled version of the Community Earth System Model, version 1.2 (iCESM1.2).

These model simulations, described in detail in Bhattacharya et al. (2022), are run with fixed SST fields in atmosphere-only mode (e.g. with the Community Atmospheric Model version 5, or iCAM5), at an 0.9°x1.25° horizontal resolution, with 30 vertical layers. While relatively low resolution, this model configuration captures the observed seasonal cycle of precipitation isotopes in the southwest (Bhattacharya et al., 2022). SSTs are taken from a pre-industrial control simulation for the 'control' experiment, while for the experimental run, SSTs are taken from a mid-to-late Pliocene simulation of CESM2 presented in Feng et al. (2020), with 2° of uniform warming added on top of this SST pattern. We refer to this as the 'relaxed gradient experiment' This simulation produces poleward amplified warming over the North Pacific, with the strongest temperature anomalies in the Bering Sea, northwest Pacific, and Gulf of Alaska (Figure 8). There is also a small warming of the cold tongue in the eastern equatorial Pacific. This simulation should therefore not be taken as a realistic simulation of the late Pliocene/early Pleistocene, but rather as a sensitivity experiment to analyze the response of regional hydroclimates to large-scale SST gradients. The pattern of SST change in the experimental simulation is different than the SST anomalies we think occurred between 2.6 and 2.0 Ma, which primarily involved poleward amplified warming and a relaxed latitudinal gradient without a distinct shift in equatorial Pacific temperatures (Figure S2). Nonetheless, our experimental simulation is still useful for exploring how regional hydroclimate responds to a relaxed latitudinal temperature gradient, helping us investigate the hypothesis that latitudinal gradients helped drive rainfall changes between 2.6 and 2.0 Ma.

Compared to the pre-industrial control, our relaxed gradient experiment produces wintertime drying over southwestern North America and wetter conditions poleward over 40°N. This is accompanied by an anomalous cyclonic circulation in the northeast Pacific, as well as a weakening of westerly winds near 60°N as well as equatorward of the low pressure center, near 25°N. While the low pressure could result from teleconnection patterns triggered by warming of the equatorial Pacific cold tongue, the rainfall pattern in Figure 8 does not resemble a canonical ENSO teleconnection pattern, which would predict wetter conditions in southwest North America in the wintertime (Goldner et al., 2011). We suggest that the poleward shift in rainfall results from a poleward shift of storm tracks in response to a relaxed latitudinal gradient. This in turn drives decreased cool season rainfall in the region around Clayton Valley, which sits on the edge of the region experiencing drying in this relatively low-resolution model simulation. A spatial average of rainfall anomalies in the region around Clayton Valley (30 to 38°N and 120 to 100°W) shows that the region indeed experiences a decrease in cool season rainfall, especially in October and November as well as in February-April, and a slight increase in summer rainfall. This is consistent with our conceptual explanation of the CV leaf wax record in section 4.2.

In the relaxed gradient experiment, precipitation isotopes are heavier in all months relative to pre-industrial (Figure 8c), likely as a result of overall warmer temperatures. These results are broadly consistent with our interpretation of the shift to more positive δD_p between 2.6 and 2.0 Ma: a decrease in the relative proportion of winter rainfall, which tends to be more isotopically depleted, and an increase in summer rainfall, which is typically more enriched in deuterium, would result in a shift to more enriched δD_p values. This would be further enhanced by an overall shift to more enriched δD_p values in all months of the year. While isotope-enabled models do not capture all the microphysical processes that influence precipitation isotopes (e.g. distinct signatures of convective versus stratiform rainfall) (Hu et al., 2018), the results of this simulation are broadly consistent with our dynamical interpretation of the Clayton Valley record. Given this simulation, and our independent proxy evidence of a relaxed latitudinal gradient of temperature between 2.6 and 2.0 Ma, we suggest that this time period was characterized by a decrease in winter storms in southwestern North America, largely as the result of a poleward shift of the jet driven by a shallower meridional temperature gradient. This decrease in winter rainfall was superimposed on a long-term trend towards decreasing summer rainfall over the Plio-Pleistocene transition (Bhattacharya et al., 2022).

4.5. Implications for Li Resources

The CV Plio-Pleistocene stable isotope records, from both carbonates and leaf waxes, suggests that the interval between 2.6 and 2.0 Ma was a time of hydroclimatic reorganization, within a broader climatic transition over the Pliocene to the Pleistocene. This involved a shift from a larger contribution of summer rainfall in the Pliocene, punctuated by a reduced contribution of winter rainfall between 2.6 and 2.0 Ma, as inferred from our proxy records and supported by model simulations. A comparison to bulk sedimentological properties suggests that the maximum concentrations of sedimentary lithium occur at roughly 2.6-2.5 Ma, and that there is a slow downward trend in lithium accumulations in sediments after 2.0 Ma (Figure 9). Here, we infer a process-based link based on the long term trends and short term variations from EXP2's carbonate and leaf wax stable isotope records, lithology, and whole rock lithium dataset.

First, the leaf wax δD_p record indicates a decrease of at least $20\,‰$ to as much as $50\,‰$ from 2.6 Ma to present. Similarly, after an initial increase from 2.9 to 2.6 Ma, the least evaporatively enriched $\delta^{18}O_{carb}$ values across the carbonate stable isotope timeseries decline approximately $7\,‰$ from 2.6 Ma to present ((Figure 9). Assuming scaling similar to the global meteoric water line (e.g. 1:8 ratio of $\delta^{18}O$ to δD), a $7\,‰$ decline in $\delta^{18}O$ is greater than would be inferred from a $20\,‰$ decrease in δD_p. However, it would be a majority of the signal inferred from a $50\,‰$ decrease in δD_p. As such, this confirms previous interpretations that the lightest $\delta^{18}O_{carb}$ values represented relatively unevaporated meteoric waters (Gagnon et al., 2023) and the periods of the greatest $\delta^{18}O_{carb}$ was likely caused by enhanced evaporation.

Second, our new measurements of lithium concentrations and carbonate stable isotope data suggest that the period of greatest lithium accumulation occurs during a time period of hydroclimate transition and high evaporation. Enriched $\delta^{18}O_{carb}$ values and lithium concentrations are observed in both the bulk sediments (Gagnon et al., 2023) and modern brines (Coffey et al., 2021). Across the record, evapoconcentration of lake water appears to drive carbonate oxygen isotopes towards higher values (due to the preferential evaporation of oxygen-16) and concentrate lithium in the paleolake in Clayton Valley. Even including our new data, the correlation between $\delta^{18}O_{carb}$ and Li concentrations remains strong (r=0.54), similar to the correlations in Gagnon et al. (2023). During the period of inferred hydroclimate reorganization based on the new leaf wax datasets, bulk lithium concentrations are between 500 and 2,000 ppm (upper continental crust is 35 ppm; Teng et al. (2004)) and are at their highest sustained values between 2.3 and 2.6 Ma.

Shifts in hydroclimate seasonality, as inferred from leaf wax δD_p data and our proxy-model comparison, would enhance lithium accumulations in the Clayton Valley paleolake. Intense summertime convective storms falling in warm conditions during the late Pliocene would favor increased weathering of the surrounding catchments driving enhanced lithium delivery to the paleolake in Clayton Valley. Warm season, intense rainfall would likely drive stronger weathering than cool season precipitation. This is supported by the strong association of lithium with clay minerals in EXP2 (Coffey et al., 2021; Gagnon et al., 2023). Reduced winter rainfall (e.g. at 2.6 Ma) would enhance wintertime evaporative demand from the lake, pushing carbonate oxygen isotopic values to heavier values and increasing solute concentrations in the paleolake and regional soil and groundwater. Furthermore, hot spring contributions (Coffey et al., 2021) to the lake could have also been enhanced via increased interaction of meteoric waters delivered during intense summer storms with range bounding faults. Hotspring and groundwater contributions to lithium accumulation may have been especially important if groundwater inputs, either from local sources or interbasin flow, helped sustain high lake levels between 2.6 and 2.0 Ma despite higher wintertime evaporative demand (Coffey et al., 2021; Gagnon et al., 2023). These processes would enhance lithium transport to and evapoconcentration in the paleolake, culminating in the highest concentrations of lithium, as well as the most enriched $\delta^{18}O_{carb}$ values, between roughly 2.6 and 2.5 Ma. Subsequent to 2.0 Ma, with reductions in summer rainfall and long-term shifts to a winter-dominated signal, despite largely similar facies (lacustrine clays) until approximately 0.7 Ma, less lithium was delivered to the lake basin resulting in lower bulk lithium values.

Non-climatic changes could also have influenced lithium. It is possible that local tectonics exposed lithium-rich source rocks at roughly 2.6 Ma, enhancing lithium delivery via enhanced weathering of the basin's watersheds. While this remains possible, after 2.9 Ma the only major lithologic change in sediments occurs at approximately 800 ka (Gagnon et al., 2023), as sedimentation from the basin's alluvial fans increasingly encroach on the EXP 2 core location. From 800 ka to present, dilution due to coarser grain sized alluvial fan sediments may be the source of whole rock lithium concentrations decreasing. Further sedimentological and geochemical analyses from depocenter cores (to the northwest of EXP2), and on clay separates, would be necessary to test the possibility of local tectonics influencing lithium delivery to the basin's lacustrine sediments. However, as the large-scale lithium concentration trends in EXP 2 are mirrored in two other deep cores covering the same time interval from the southern sub-basin of CV (Coffey et al., 2021) we propose that the CV sediments record a wholesale response to hydroclimate in the lithium concentration trends observed with depth.

Given these observations linking the carbonate and leaf wax stable isotope records to lithium accumulation in the EXP2 core, we contend that rainfall seasonality driving weathering reactions on the landscape likely played an important role, in addition to evapoconcentration of the paleolake, in lithium enrichment in Clayton Valley. Such a process-based link is likely to be found in other closed basins with lithium rich clay deposits.

5. Conclusions

In this paper, we presented a new Plio-Pleistocene record of leaf wax carbon and hydrogen isotopes from Clayton Valley, Nevada. This record, which spans the interval from approximately 2.8 Ma to the present, provides an unprecedented view of changes in the seasonality of rainfall from the Great Basin. Analyses of 3 different chain lengths of leaf waxes show a shift to more enriched values between roughly 2.6 and 2.0 Ma, at the start of the Quaternary and coincident with global cooling and the inception of northern hemisphere glaciation. This interval is also characterized by more positive values of δ^{18}O of authigenic carbonate, and an increase in lithium concentrations in sediments. Other regional leaf wax records also include an excursion to more positive δD_p values in this interval. We interpret this positive shift as a northward shift or a decrease in the intensity of winter storm tracks, resulting in summer rainfall providing a greater share of annual rainfall. This pattern is super-imposed on a long-term decline in summertime rainfall from 3.0 to roughly 2.0-2.5 Ma.

Warming in the high latitude Pacific Ocean likely contributed to the reduction in winter rainfall at the start of the Pleistocene. In modern observational data, cool SST anomalies in the Gulf of Alaska and Bering Sea is linked to an increase in winter storm activity over western North America, while anomalously warm temperatures reduce transient eddy activity. While only a few continuous SST records are available from the Plio-Pleistocene high northern latitude Pacific, available data does suggest a relaxation of the latitudinal temperature gradient between 2.6 and 2.0 Ma. This would support a reduction in North Pacific storm activity within this interval, though more data is needed to precisely constrain SST gradients. We find support for this view in a simulation of the isotope-enabled Community Atmospheric Model (iCAM5) which, when forced with a relaxed meridional temperature gradient in the Pacific, results in a northward shift in wintertime storm activity and a drying of the region near Clayton Valley and ODP 1012. In this simulation, δD_p becomes more enriched, partially as a result of an increase in enriched summer rainfall and a decrease in depleted winter rainfall. There is also an increase in the isotopic signature of rainfall in all months, likely as a result of overall warmer temperatures in the uniform warming compared to the pre-industrial simulation.

Overall, our results suggest that the Plio-Pleistocene transition involved a significant reorganization of rainfall regimes in southwestern North America. While previous studies have shown that the Pliocene was characterized by a greater proportion of summer rainfall, the record from CV, along with our SST compilation and model simulation, suggest that, instead of a steady long-term trend to a greater dominance of winter rainfall in the southern Great Basin, the late Pliocene and early Pleistocene featured a punctuated climatic interval between 2.0 and 2.6 Ma with reduced winter rainfall. This underscores the sensitivity of rainfall in western North America to large-scale SST gradients. Further work to constrain the dynamics of winter rainfall changes over the Plio-Pleistocene could provide constraints on the sensitivity of precipitation regimes in western North America to large-scale shifts in past and future SST patterns.

Finally, it is notable that the interval between 2.6 and 2.0 Ma coincides with a time period of greater enrichment of lithium in the CV lake sediments, highlighting the long-term coupling of hydroclimatic regime changes and the formation of economically important lithium-rich brines and claystones in the desert southwest. Our combined interpretation of existing inorganic geochemical proxies and our organic proxies suggests that it was not just aridity that exerted an important influence on the development of lithium resources in the southwest, but rather a shift in the seasonality of the rainfall regimes. Our work therefore highlights the long-term coupling between precipitation seasonality, and hydroclimate more generally, with the formation of economically important deposits of a key 21st century critical mineral.

6. Acknowledgments

TB acknowledges funding from NSF P2C2 Grant OCE-1903148 and NSF CAREER Award OCE-2237502. DEI acknowledges funding from NSF P2C2 grant AGS-2102901 and the Institute at Brown for Environment and Society. We thank Bryce Belanger (Vanderbilt) and Matthew Bolton (University of Alberta) for field assistance and help identifying ash layers in cores from CV. Andrew Cooper (Thermo) and Christopher Maupin (Texas A&M) provided essential instrumentation support. We thank Albemarle Corporation for providing logistical support and access to cores. Leaf wax data and new carbonate and lithium data is permanently archived in the NOAA Paleoclimatology Database upon acceptance of this manuscript.

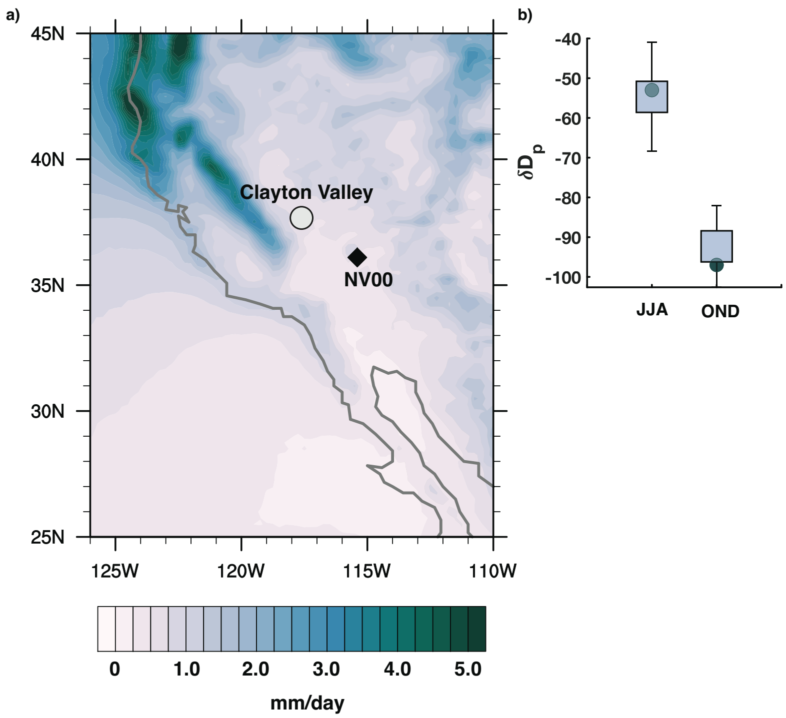

Figure 1: **Study region and background climatology.** a) Background colors indicate annual average rainfall rates over western US, with the location of Clayton Valley (CV) and the isotope monitoring site (NV-00) indicated on the map. b) shows amount-weighted estimate of δD of precipitation in summer (JJA) and winter (OND) from NV-00 (Welker, 2012) in boxplots with 1-σ error bars, with circles indicating estimated seasonal precipitation isotopic composition from the Online Isotopes in Precipitation Calculator (Bowen and Revenaugh, 2003). Seasonal intervals chosen to maximize the data availability at the NV-00 data (e.g. very little data from September was available).

References

Aggarwal, P.K., Romatschke, U., Araguas-Araguas, L., Belachew, D., Longstaffe, F.J., Berg, P., Schumacher, C., Funk, A., 2016. Proportions of convective and stratiform precipitation revealed in water isotope ratios. Nature Geoscience 9, 624–629.

Almazroui, M., Islam, M.N., Saeed, F., Saeed, S., Ismail, M., Ehsan, M.A.,

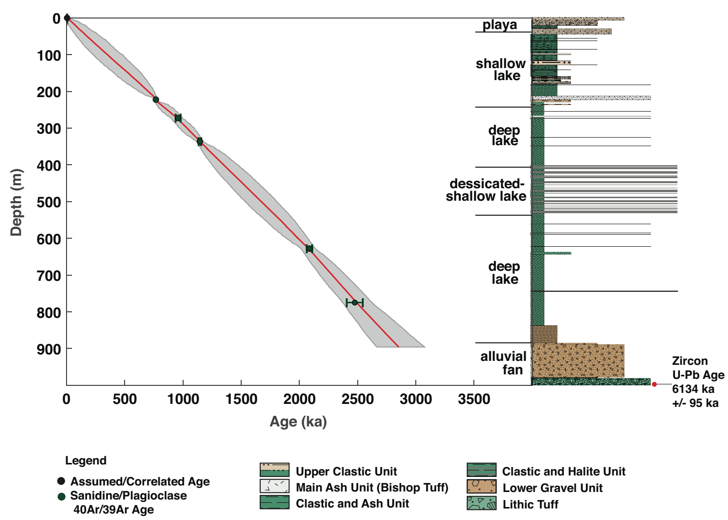

Figure 2: **Age model and stratigraphy for EXP2 core from Clayton Valley.** Left panel shows age model based on five dates and an assumed surface age, with stratigraphy shown to the right. This plot is modified with permission from Gagnon et al. (2023).

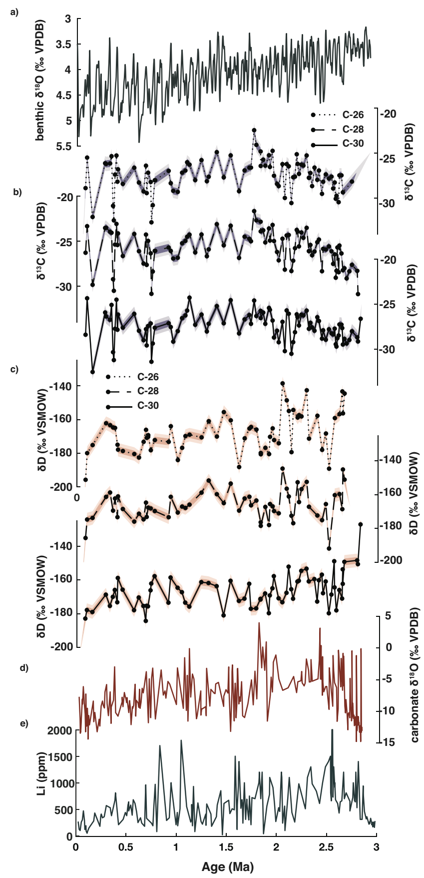

Figure 3: **Raw isotopic data from Clayton Valley**. a) shows the benthic oxygen isotope stack from Westerhold et al. (2020) for context. Panel b) shows carbon isotopic data from three long-chain leaf waxes (e.g. the C-26, C-28, and C-30) alkanoic acid); while c) shows hydrogen isotopic data from the same leaf wax chain lengths. d) shows previously published oxygen isotope data from authigenic lacustrine carbonates from Gagnon et al. (2023), supplemented with additional data, while e) shows Li concentration data from the Clayton Valley core, from Gagnon et al. (2023) and Coffey et al. (2021), with some new data reported in this study. Note age uncertainty is not plotted in these timeseries.

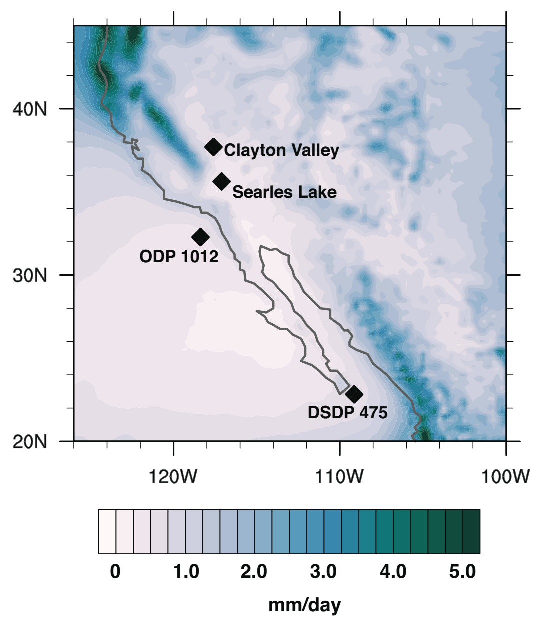

Figure 4: **Location of Plio-Pleistocene δD of precipitation reconstructions**. Clayton Valley data is from this study, while ODP 1012 and c) DSDP 475 were published in Bhattacharya et al. (2022). A shorter high-resolution record from Searles Valley is published in Peaple et al. (2024).

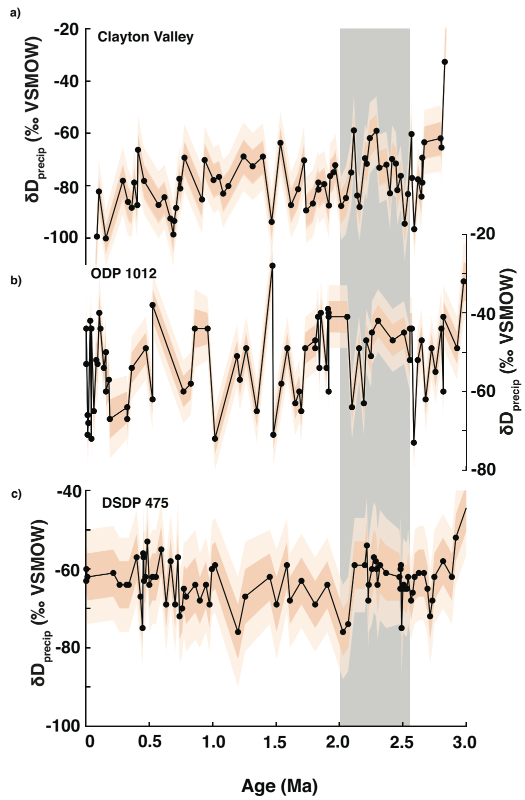

Figure 5: **Leaf wax δD of precipitation reconstructions from southwestern North America**. a) shows Clayton Valley record, presented in this paper. Error bars for this record include age uncertainty, analytical uncertainty, as well as the uncertainty introduced by our method for reconstructing δD_p. b) and c) show the records from ODP 1012 and DSDP 475, presented in (Bhattacharya et al., 2022). All records are based on the C_{30} *n*-acid.

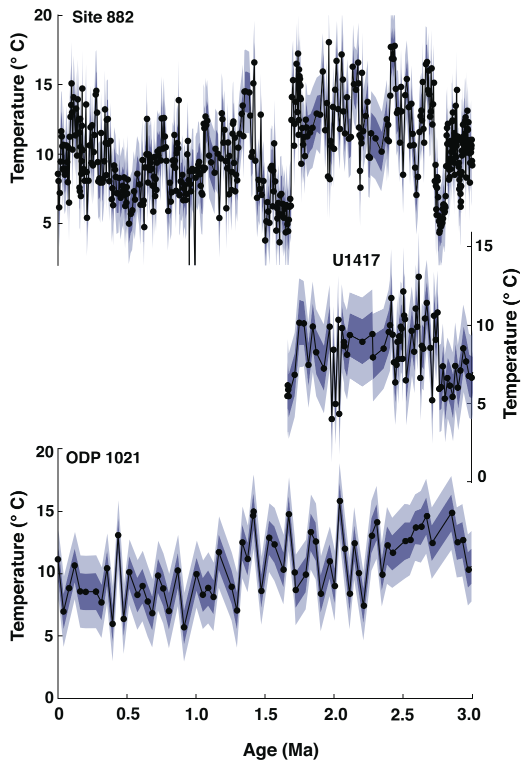

Figure 6: **East Pacific extratropical SST records covering the interval from 3.0 Ma to present**. a) shows the record from the western Bering Sea from Site 882 (Yamamoto and Kobayashi, 2016); b) shows the record from U1417 in the Gulf of Alaska (Sánchez-Montes et al., 2020)l while c) shows Site 1021 on the northern California Margin (LaRiviere et al., 2012).

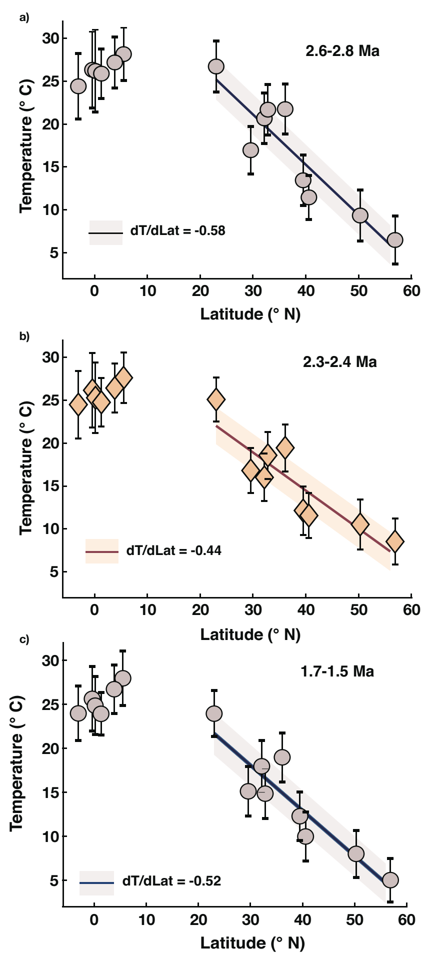

Figure 7: **Pacific Latitudinal SST Gradients prior to and during early Pleistocene**. a) shows the extratropical meridional temperature gradient between 2.6 and 2.8 Ma. b) shows the gradient between 2.3 and 2.4 Ma, during the interval when we observe rising values of δD_p at CV. c) shows the meridional gradient during the interval between 1.5 and 1.7 Ma. For all three intervals, a least-squares regression line is calculated between 20 and 60 ° N, and the slope is shown in the bottom left of the panel. Error envelopes represent 95% confidence interval calculated from iterating through full range of calibrated SST data. The slope is significantly shallower between 2.3 and 2.4 Ma compared to the interval before (2.6 to 2.8 Ma) and after (1.5 to 1.7 Ma) at the 95% level. See text for more details on the SST proxy compilation.

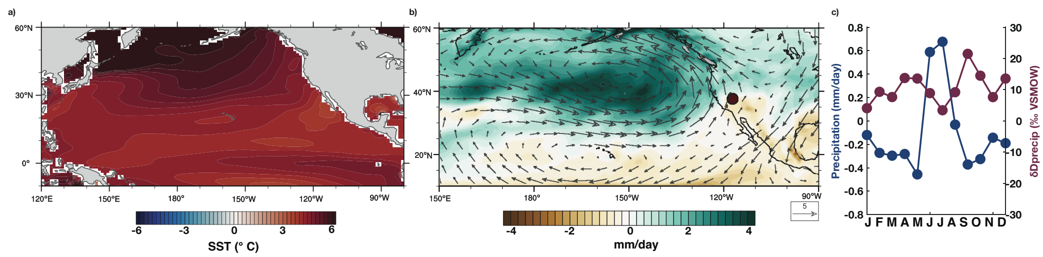

Figure 8: **Atmospheric Changes in iCAM5 in PI Control compared to Pliocene pattern plus 2x warming Experimental run**. a) SST difference between relaxed gradient experimental simulation and PI (1xCO_2) simulation. See text for details on experimental set up. b) Winter (DJF) precipitation as well as 850 mb wind differences between these simulations; c) Differences of monthly precipitation (blue) and δD_p (maroon) between these simulations.

Diallo, I., O'Brien, E., Ashfaq, M., Martínez-Castro, D., Cavazos, T., Cerezo-Mota, R., Tippett, M.K., Gutowski, W.J., Alfaro, E.J., Hidalgo, H.G., Vichot-Llano, A., Campbell, J.D., Kamil, S., Rashid, I.U., Sylla, M.B., Stephenson, T., Taylor, M., Barlow, M., 2021. Projected Changes in Temperature and Precipitation Over the United States, Central America, and the Caribbean in CMIP6 GCMs. Earth Systems and Environment 5, 1–24. URL: `http://link.springer.com/10.1007/s41748-021-00199-5`, doi:10.1007/s41748-021-00199-5.

Beaudin, É., Di Lorenzo, E., Miller, A., Seo, H., Joh, Y., 2023. Impact of Extratropical Northeast Pacific SST on US West Coast Precipitation. Geophysical Research Letters 50, e2022GL102354.

Benson, T.R., Coble, M.A., Dilles, J.H., 2023. Hydrothermal enrichment of lithium in intracaldera illite-bearing claystones. Science Advances 9, eadh8183.

Bhattacharya, T., Feng, R., Maupin, C.R., Coats, S., Brennan, P.R.,

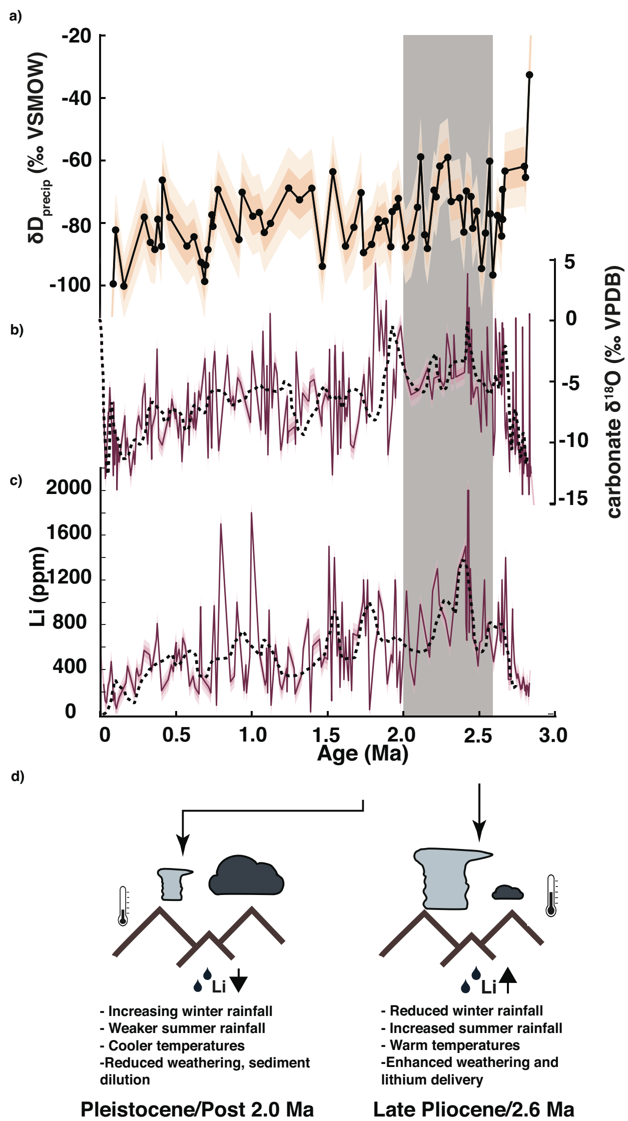

Figure 9: **Summary of environmental changes at CV and relationship to lithium enrichment**. a) δD_p reconstruction from Clayton Valley with all sources of uncertainty incorporated into 1-σ (darker) and 2-σ (lighter) uncertainty envelopes (e.g. as in Figure 5) b) authigenic carbonate oxygen isotope data and c) bulk sediment lithium concentration in ppm (oxygen isotope data and lithium concentrations are previously shown in Figure 3). Light (2-σ) and dark error (1-σ) envelopes represent the combined influence of age and analytical uncertainty. In panels b) and c), a low pass butterworth filtered version of the data is shown in a dashed black line. d) summary cartoon of climate changes in late Pliocene (roughly 2.6 Ma) and the Pleistocene during the interval after 2.0 Ma.

Carter, E., 2023. California margin temperatures modulate regional circulation and extreme summer precipitation in the desert Southwest. Environmental Research Letters 18, 104048. URL: https://iopscience.iop.org/article/10.1088/1748-9326/acfd43, doi:10.1088/1748-9326/acfd43.

Bhattacharya, T., Feng, R., Tierney, J.E., Rubbelke, C., Burls, N., Knapp, S., Fu, M., 2022. Expansion and intensification of the North American Monsoon during the Pliocene. AGU Advances 3, e2022AV000757.

Bhattacharya, T., Tierney, J.E., Addison, J.A., Murray, J.W., 2018. Ice-sheet modulation of deglacial North American monsoon intensification. Nature Geoscience 11, 848–852.

Blaauw, M., Christen, J.A., Bennett, K., Reimer, P.J., 2018. Double the dates and go for Bayes—Impacts of model choice, dating density and quality on chronologies. Quaternary Science Reviews 188, 58–66.

Bowen, G.J., Revenaugh, J., 2003. Interpolating the isotopic composition of modern meteoric precipitation. Water resources research 39.

Brennan, P.R., Bhattacharya, T., Feng, R., Tierney, J.E., Jorgensen, E.M., 2022. Patterns and mechanisms of northeast Pacific temperature response to Pliocene boundary conditions. Paleoceanography and Paleoclimatology 37, e2021PA004370.

Brierley, C.M., Fedorov, A.V., Liu, Z., Herbert, T.D., Lawrence, K.T., LaRiviere, J.P., 2009. Greatly expanded tropical warm pool and weakened Hadley circulation in the early Pliocene. Science 323, 1714–1718.

Burls, N.J., Fedorov, A.V., Sigman, D.M., Jaccard, S.L., Tiedemann, R., Haug, G.H., 2017. Active Pacific meridional overturning circulation (PMOC) during the warm Pliocene. Science Advances 3, e1700156.

Chikaraishi, Y., Naraoka, H., 2006. Carbon and hydrogen isotope variation of plant biomarkers in a plant–soil system. Chemical Geology 231, 190–202.

Choi, J., Lu, J., Son, S., Frierson, D.M.W., Yoon, J., 2016. Uncertainty in future projections of the North Pacific subtropical high and its implication for California winter precipitation change. Journal of Geophysical Research: Atmospheres 121, 795–806. URL: https://onlinelibrary.wiley.com/doi/10.1002/2015JD023858, doi:10.1002/2015JD023858.

Coffey, D., Munk, L.A., Ibarra, D., Butler, K., Boutt, D., Jenckes, J., 2021. Lithium storage and release from lacustrine sediments: Implications for lithium enrichment and sustainability in continental brines. Geochemistry, Geophysics, Geosystems 22, e2021GC009916.

Collister, J.W., Rieley, G., Stern, B., Eglinton, G., Fry, B., 1994. Compound-specific δ 13C analyses of leaf lipids from plants with differing carbon dioxide metabolisms. Organic geochemistry 21, 619–627.

Cook, B.I., Seager, R., 2013. The response of the North American Monsoon to increased greenhouse gas forcing: NA MONSOON AND GHG WARMING. Journal of Geophysical Research: Atmospheres 118, 1690–1699. URL: http://doi.wiley.com/10.1002/jgrd.50111, doi:10.1002/jgrd.50111.

Davis, J.R., Friedman, I., Gleason, J., 1986. Origin of the lithium-rich brine, clayton valley, nevada. US Geological Survey Bulletin 1622, 131–138.

Dekens, P.S., Ravelo, A.C., McCarthy, M.D., 2007. Warm upwelling regions in the pliocene warm period. Paleoceanography 22.

Donovan, L., Ehleringer, J., 1994. Water stress and use of summer precipitation in a Great Basin shrub community. Functional Ecology , 289–297.

Eastoe, C., Dettman, D., 2016. Isotope amount effects in hydrologic and climate reconstructions of monsoon climates: Implications of some long-term data sets for precipitation. Chemical Geology 430, 78–89.

Etourneau, J., Schneider, R., Blanz, T., Martinez, P., 2010. Intensification of the Walker and Hadley atmospheric circulations during the Pliocene–Pleistocene climate transition. Earth and Planetary Science Letters 297, 103–110. URL: https://www.sciencedirect.com/science/article/pii/S0012821X10003845, doi:10.1016/j.epsl.2010.06.010.

Feng, R., Otto-Bliesner, B.L., Brady, E.C., Rosenbloom, N., 2020. Increased climate response and Earth system sensitivity from CCSM4 to CESM2 in mid-

Pliocene simulations. Journal of Advances in Modeling Earth Systems 12, e2019MS002033.

Friedman, I., Smith, G.I., Johnson, C.A., Moscati, R.J., 2002. Stable isotope compositions of waters in the Great Basin, United States 2. Modern precipitation. Journal of Geophysical Research: Atmospheres 107, ACL–15.

Gagnon, C.A., Butler, K.L., Gaviria, E., Terrazas, A., Gao, A., Bhattacharya, T., Boutt, D.F., Munk, L.A., Ibarra, D.E., 2023. Paleoclimate controls on lithium enrichment in Great Basin Pliocene- Pleistocene lacustrine clays. Geological Society of America Bulletin .

Gan, B., Wu, L., 2013. Seasonal and Long-Term Coupling between Wintertime Storm Tracks and Sea Surface Temperature in the North Pacific. Journal of Climate 26, 6123–6136. URL: `http://journals.ametsoc.org/doi/10.1175/JCLI-D-12-00724.1`, doi:10.1175/JCLI-D-12-00724.1.

Gan, B., Wu, L., Jia, F., Li, S., Cai, W., Nakamura, H., Alexander, M.A., Miller, A.J., 2017. On the response of the Aleutian low to greenhouse warming. Journal of Climate 30, 3907–3925.

Gao, L., Edwards, E.J., Zeng, Y., Huang, Y., 2014. Major evolutionary trends in hydrogen isotope fractionation of vascular plant leaf waxes. PloS one 9, e112610.

Giamalaki, K., Beaulieu, C., Henson, S.A., Martin, A.P., Kassem, H., Faranda, D., 2021. Future intensification of extreme Aleutian low events and their climate impacts. Scientific Reports 11, 18395. URL: https://www.nature.com/articles/s41598-021-97615-7, doi:10.1038/s41598-021-97615-7.

Goldner, A., Huber, M., Diffenbaugh, N., Caballero, R., 2011. Implications of the permanent El Niño teleconnection" blueprint" for past global and North American hydroclimatology. Climate of the Past 7, 723–743.

Harada, N., Sato, M., Shiraishi, A., Honda, M.C., 2006. Characteristics of alkenone distributions in suspended and sinking particles in the northwestern North Pacific. Geochimica et Cosmochimica Acta 70, 2045–2062.

Herbert, T.D., Lawrence, K.T., Tzanova, A., Peterson, L.C., Caballero-Gill, R., Kelly, C.S., 2016. Late Miocene global cooling and the rise of modern ecosystems. Nature Geoscience 9, 843–847. URL: https://www.nature.com/articles/ngeo2813, doi:10.1038/ngeo2813. number: 11 Publisher: Nature Publishing Group.

Herbert, T.D., Schuffert, J.D., 2000. 16. alkenone unsaturation estimates of sea-surface temperatures at site 1002 over a full glacial cycle, in: Proceedings of the Ocean Drilling Program, Scientific Results, pp. 239–247.

Hu, J., Emile-Geay, J., Nusbaumer, J., Noone, D., 2018. Impact of Convective

Activity on Precipitation δ 18O in Isotope-Enabled General Circulation Models. Journal of Geophysical Research: Atmospheres 123, 13–595.

Ibarra, D.E., Oster, J.L., Winnick, M.J., Caves Rugenstein, J.K., Byrne, M.P., Chamberlain, C.P., 2018. Warm and cold wet states in the western United States during the Pliocene–Pleistocene. Geology 46, 355–358.

Inglis, G.N., Bhattacharya, T., Hemingway, J.D., Hollingsworth, E.H., Feakins, S.J., Tierney, J.E., 2022. Biomarker approaches for reconstructing terrestrial environmental change. Annual Review of Earth and Planetary Sciences 50, 369–394.

King, K.E., Cook, E.R., Anchukaitis, K.J., Cook, B.I., Smerdon, J.E., Seager, R., Harley, G.L., Spei, B., 2024. Increasing prevalence of hot drought across western North America since the 16th century. Science Advances 10, eadj4289.

Kukla, T., Rugenstein, J., Ibarra, D.E., Winnick, M., Strömberg, C.A., Chamberlain, C., 2022. Drier winters drove Cenozoic open habitat expansion in North America. AGU Advances 3, e2021AV000566.

LaRiviere, J.P., Ravelo, A.C., Crimmins, A., Dekens, P.S., Ford, H.L., Lyle, M., Wara, M.W., 2012. Late Miocene decoupling of oceanic warmth and atmospheric carbon dioxide forcing. Nature 486, 97–100.

Lawrence, K.T., Liu, Z., Herbert, T.D., 2006. Evolution of the Eastern Tropical Pacific Through Plio-Pleistocene Glaciation. Science 312, 79–83. URL: `https://science.sciencemag.org/content/312/5770/79`, doi:10.1126/science.1120395. publisher: American Association for the Advancement of Science Section: Research Article.

Lechler, A.R., Galewsky, J., 2013. Refining paleoaltimetry reconstructions of the Sierra Nevada, California, using air parcel trajectories. Geology 41, 259–262.

Lisiecki, L.E., Raymo, M.E., 2005. A Pliocene-Pleistocene stack of 57 globally distributed benthic δ18O records. Paleoceanography 20.

Liu, J., An, Z., 2020. Leaf wax n-alkane carbon isotope values vary among major terrestrial plant groups: Different responses to precipitation amount and temperature, and implications for paleoenvironmental reconstruction. Earth-Science Reviews 202, 103081.

Liu, J., Tian, J., Liu, Z., Herbert, T.D., Fedorov, A.V., Lyle, M., 2019. Eastern equatorial Pacific cold tongue evolution since the late Miocene linked to extratropical climate. Science Advances 5, eaau6060. URL: https://advances.sciencemag.org/content/5/4/eaau6060, doi:10.1126/sciadv.aau6060. publisher: American Association for the Advancement of Science Section: Research Article.

Menemenlis, S., Lora, J.M., Lofverstrom, M., Chandan, D., 2021. Influence of stationary waves on mid-Pliocene atmospheric rivers and hydroclimate. Global and Planetary Change 204, 103557. URL: https://linkinghub.elsevier.com/retrieve/pii/S0921818121001429, doi:10.1016/j.gloplacha.2021.103557.

Mix, H.T., Caves Rugenstein, J.K., Reilly, S.P., Ritch, A.J., Winnick, M.J., Kukla, T., Chamberlain, C.P., 2019. Atmospheric flow deflection in the late cenozoic sierra nevada. Earth and Planetary Science Letters 518, 76–85. URL: `http://dx.doi.org/10.1016/j.epsl.2019.04.050`, doi:10.1016/j.epsl.2019.04.050.

Munk, L., Chamberlain, C.P., 2011. Final technical report: G10ap00056-lithium brine resources: A predictive exploration model. Research supported by the US Geological Survey (USGS), Department of the Interior, under USGS award .

Munk, L.A., Hynek, S.A., Bradley, D.C., Boutt, D., Labay, K., Jochens, H., 2016. Lithium Brines, a global perspective. Society of Economic Geologists. URL: `http://dx.doi.org/10.5382/Rev.18.14`, doi:10.5382/rev.18.14.

Pascale, S., Boos, W.R., Bordoni, S., Delworth, T.L., Kapnick, S.B., Murakami, H., Vecchi, G.A., Zhang, W., 2017. Weakening of the North American monsoon with global warming. Nature Climate Change 7, 806–812. URL: `https://www.nature.com/articles/nclimate3412`, doi:10.1038/nclimate3412.

Peaple, M.D., Bhattacharya, T., Lowenstein, T.K., McGee, D., Olson, K.J., Stroup, J.S., Tierney, J.E., Feakins, S.J., 2022. Biomarker and pollen evidence for late Pleistocene pluvials in the Mojave Desert. Paleoceanography and Paleoclimatology 37, e2022PA004471.

Peaple, M.D., Bhattacharya, T., Tierney, J.E., Knott, J.R., Lowenstein, T.K., Feakins, S.J., 2024. Biomarker evidence for an MIS M2 Glacial-Pluvial in the Mojave Desert before warming and drying in the late Pliocene. Paleoceanography and Paleoclimatology 39, e2023PA004687. URL: https://agupubs.onlinelibrary.wiley.com/doi/10.1029/2023PA004687, doi:10.1029/2023PA004687.

Pickart, R.S., Macdonald, A.M., Moore, G.W.K., Renfrew, I.A., Walsh, J.E., Kessler, W.S., 2009. Seasonal Evolution of Aleutian Low Pressure Systems: Implications for the North Pacific Subpolar Circulation*. Journal of Physical Oceanography 39, 1317–1339. URL: http://journals.ametsoc.org/doi/10.1175/2008JPO3891.1, doi:10.1175/2008JPO3891.1.

Rousselle, G., Beltran, C., Sicre, M.A., Raffi, I., De Rafélis, M., 2013. Changes in sea-surface conditions in the Equatorial Pacific during the middle Miocene–Pliocene as inferred from coccolith geochemistry. Earth and Planetary Science Letters 361, 412–421. URL: https://www.sciencedirect.com/science/article/pii/S0012821X12006115, doi:10.1016/j.epsl.2012.11.003.

Sachse, D., Billault, I., Bowen, G.J., Chikaraishi, Y., Dawson, T.E., Feakins, S.J., Freeman, K.H., Magill, C.R., McInerney, F.A., Van Der Meer, M.T., et al., 2012. Molecular paleohydrology: interpreting the hydrogen-isotopic composition of lipid biomarkers from photosynthesizing organisms. Annual Review of Earth and Planetary Sciences 40, 221–249.

Sachse, D., Radke, J., Gleixner, G., 2004. Hydrogen isotope ratios of recent lacustrine sedimentary n-alkanes record modern climate variability. Geochimica et Cosmochimica Acta 68, 4877–4889.

Sage, R.F., Wedin, D.A., Li, M., et al., 1999. The biogeography of c4 photosynthesis: patterns and controlling factors. C4 plant biology 10, 313–376.

Sánchez-Montes, M.L., McClymont, E.L., Lloyd, J.M., Müller, J., Cowan, E.A., Zorzi, C., 2020. Late Pliocene Cordilleran Ice Sheet development with warm northeast Pacific sea surface temperatures. Climate of the Past 16, 299–313.

Schrag, D.P., Hampt, G., Murray, D.W., 1996. Pore fluid constraints on the temperature and oxygen isotopic composition of the glacial ocean. Science 272, 1930–1932.

Schumacher, C., Funk, A., 2023. Assessing Convective-Stratiform Precipitation Regimes in the Tropics and Extratropics With the GPM Satellite Radar. Geophysical Research Letters 50, e2023GL102786.

Seki, O., Schmidt, D.N., Schouten, S., Hopmans, E.C., Damsté, J.S.S., Pancost, R.D., 2012. Paleoceanographic changes in the Eastern Equatorial Pacific over the last 10 Myr. Paleoceanography 27. URL: `https://agupubs.onlinelibrary.wiley.com/doi/abs/10.1029/2011PA002158`, doi:https://doi.org/10.1029/2011PA002158. _eprint: https://agupubs.onlinelibrary.wiley.com/doi/pdf/10.1029/2011PA002158.

Shaari, H.b., Yamamoto, M., Irino, T., 2013. Enhanced upwelling in the eastern equatorial Pacific at the last five glacial terminations. Palaeogeography, Palaeoclimatology, Palaeoecology 386, 8–15. URL: https://www.sciencedirect.com/science/article/pii/S0031018213001600, doi:10.1016/j.palaeo.2013.03.022.

Teng, F.Z., McDonough, W., Rudnick, R., Dalpé, C., Tomascak, P., Chappell, B., Gao, S., 2004. Lithium isotopic composition and concentration of the upper continental crust. Geochimica et Cosmochimica Acta 68, 4167–4178. URL: https://www.sciencedirect.com/science/article/pii/S0016703704004326, doi:https://doi.org/10.1016/j.gca.2004.03.031.

Thompson, R.S., 1991. Pliocene environments and climates in the western United States. Quaternary Science Reviews 10, 115–132.

Tierney, J.E., Haywood, A.M., Feng, R., Bhattacharya, T., Otto-Bliesner, B.L., 2019. Pliocene warmth consistent with greenhouse gas forcing. Geophysical Research Letters 46, 9136–9144.

Tierney, J.E., Pausata, F.S., deMenocal, P.B., 2017. Rainfall regimes of the Green Sahara. Science advances 3, e1601503.

Tierney, J.E., Tingley, M.P., 2018. BAYSPLINE: A new calibration for the alkenone paleothermometer. Paleoceanography and Paleoclimatology 33, 281–301.

Vine, J.D., 1975. Lithium in sediments and brines-how, why, and where to search. Journal of Research of the US Geological Survey 3, 479–485.

Wallace, B., Minder, J.R., 2024. The North American Monsoon precipitation response to climate warming at convection-permitting scales. Climate Dynamics 62, 497–524. URL: https://link.springer.com/10.1007/s00382-023-06920-6, doi:10.1007/s00382-023-06920-6.

Wang, L., Hu, H., Yang, X., 2019. The atmospheric responses to the intensity variability of subtropical front in the wintertime North Pacific. Climate Dynamics 52, 5623–5639. URL: http://link.springer.com/10.1007/s00382-018-4468-9, doi:10.1007/s00382-018-4468-9.

Welker, J.M., 2012. ENSO effects on δ18O, δ2H and d-excess values in precipitation across the US using a high-density, long-term network (USNIP). Rapid Communications in Mass Spectrometry 26, 1893–1898.

Westerhold, T., Marwan, N., Drury, A.J., Liebrand, D., Agnini, C., Anagnostou, E., Barnet, J.S., Bohaty, S.M., De Vleeschouwer, D., Florindo, F., et al., 2020. An astronomically dated record of Earth's climate and its predictability over the last 66 million years. Science 369, 1383–1387.

Williams, A.P., Cook, E.R., Smerdon, J.E., Cook, B.I., Abatzoglou, J.T., Bolles, K., Baek, S.H., Badger, A.M., Livneh, B., 2020. Large contribution from anthropogenic warming to an emerging North American megadrought. Science 368, 314–318.

Windler, G., Tierney, J.E., deMenocal, P.B., 2023. Hydroclimate Variability in the Equatorial Western Indian Ocean for the Last 250,000 Years. Paleoceanography and Paleoclimatology 38, e2022PA004530.

Yamamoto, M., Kobayashi, D., 2016. Surface ocean cooling in the subarctic North Pacific during the late Pliocene suggests an atmospheric reorganization prior to extensive Northern Hemisphere glaciation. Deep Sea Research Part II: Topical Studies in Oceanography 125, 177–183.

Supporting Information for "Pleistocene shifts in Great Basin hydroclimate seasonality govern the formation of lithium-rich paleolake deposits"

Tripti Bhattacharya[1], Peter R. Brennan[1], Daniel E Ibarra [2], Catherine A. Gagnon [2], Kristina L. Butler [2,6], Alexa Terrazas[6], Shaw Miller[2], Lee Ann Munk [3], David F. Boutt [4], Ran Feng[5], Stephanie N. Bullinger[1], Lucy Weisbeck[1]

[1]Department of Earth and Environmental Sciences, Syracuse University, Syracuse NY

[2]Department of Earth, Environmental and Planetary Science, Brown University, Providence, RI

[6]Department of Atmospheric and Ocean Sciences, University of California Los Angeles, Los Angeles, CA

[3]Department of Geological Sciences, University of Alaska-Anchorage, Anchorange, AK

[4]Department of Geosciences, University of Massachusetts-Amherst, Amherst, MA

[5]Department of Earth, Geographic, and Climate Sciences, University of Connecticut, Storrs, CT

[6]Department of Sustainable Earth Systems Sciences, University of Texas at Dallas, Dallas, TX

Contents of this file

Figures

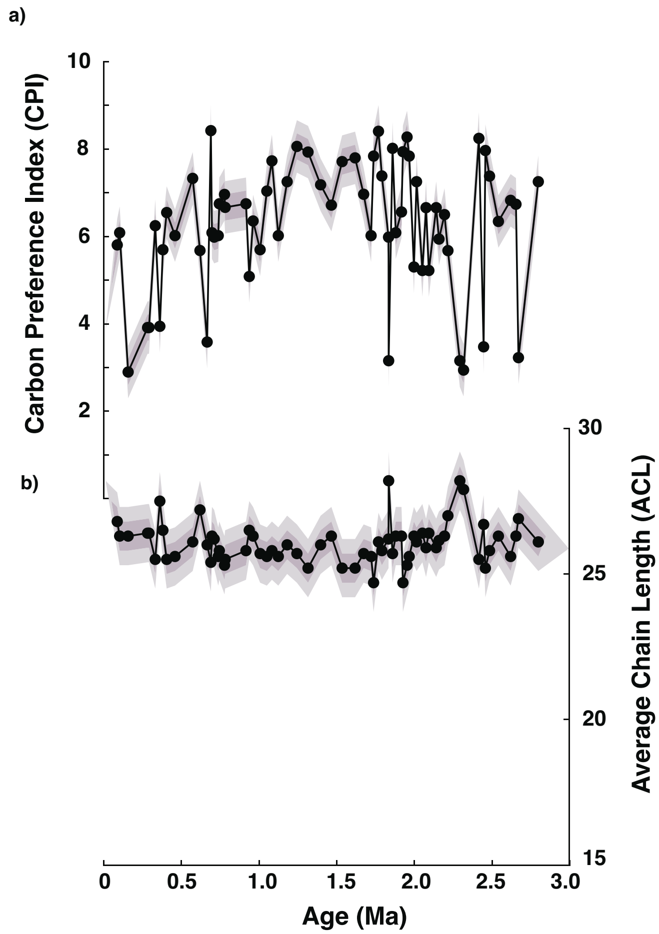

Figure S1. Average chain length (panel a) and carbon preference index (panel b) for alkanoic acids in Clayton Valley record.

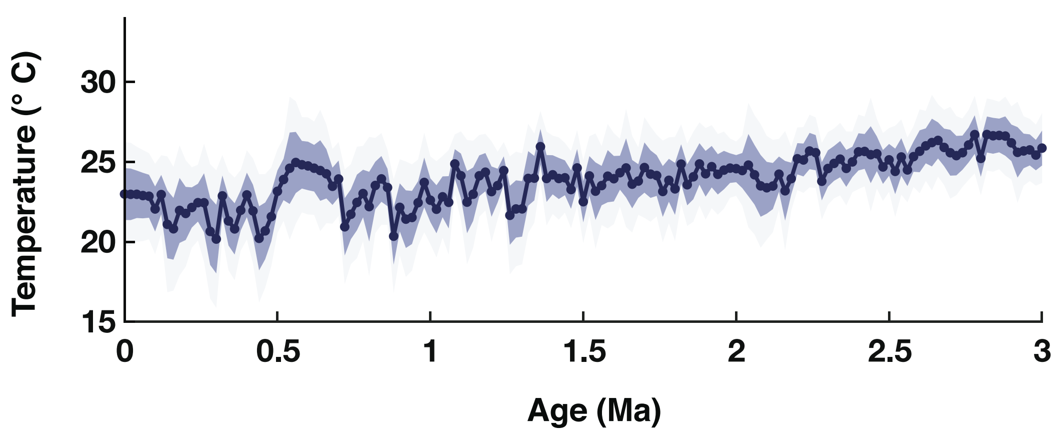

Figure S2. Evolution of temperature in the eastern equatorial Pacific cold tongue from the late Pliocene to the present. For more details on the calculation method, please see (Bhattacharya et al., 2022).

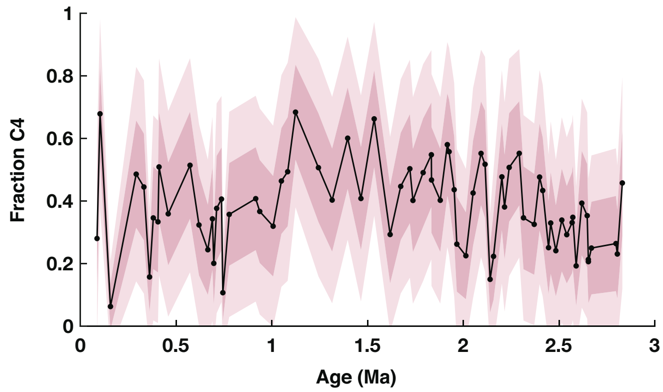

Figure S3. Calculated fraction of C4 vegetation (f_4) based on carbon isotopes of the C-30 n-acid. Dark and light error envelopes represent 1σ and 2σ uncertainties.

Tables

Table 1 Correlation matrix for timeseries of carbon (C) and hydrogen (H) of each chain length of alkanoic acid, from 26 to 30. We also analyze the correlation with carbonate δ^{18}O. Significant correlations are highlighted with an asterisk. Timeseries were interpolated to a common timestep before performing correlation analysis.

	$\mathbf{C}_{26}$	$\mathbf{C}_{28}$	$\mathbf{C}_{30}$	$\mathbf{H}_{26}$	$\mathbf{H}_{28}$	$\mathbf{H}_{30}$	$\delta^{18}\mathbf{O}_{carb}$
$\mathbf{C}_{26}$	-	0.78*	0.84*	-0.02	-0.14	-0.05	0.225
$\mathbf{C}_{28}$	x	-	0.87*	0.49*	0.41	-0.45	0.34
$\mathbf{C}_{30}$	x	x	-	-0.27	-0.28	-0.22	0.12
$\mathbf{H}_{26}$	x	x	x	-	0.65*	0.87*	-0.06
$\mathbf{H}_{28}$	x	x	x	x	-	0.64*	0.37
$\mathbf{H}_{30}$	x	x	x	x	x	-	0.07
$\delta^{18}\mathbf{O}_{carb}$	x	x	x	x	x	x	-

References

Bhattacharya, T., Feng, R., Tierney, J. E., Rubbelke, C., Burls, N., Knapp, S., & Fu, M. (2022). Expansion and intensification of the north american monsoon during the pliocene. *AGU Advances*, *3*(6), e2022AV000757.